Journal of
Materials Chemistry A

Materials for energy and sustainability

ROYAL SOCIETY
OF CHEMISTRY
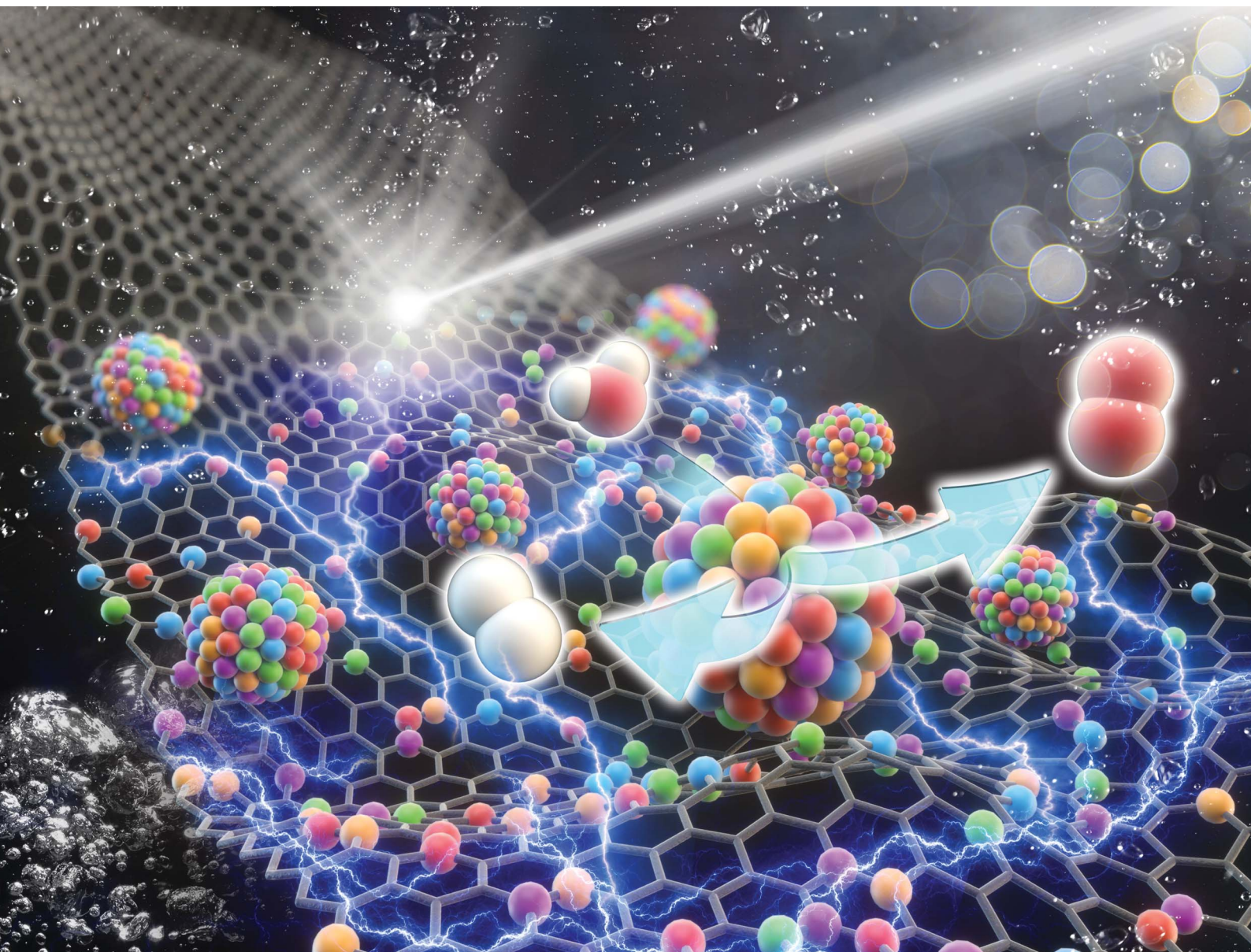
PAPER
Soorathep Kheawhom, Myong Yong Choi *et al.*
Pulsed laser-patterned high-entropy single-atomic sites
and alloy coordinated graphene oxide for pH-universal
water electrolysis

Check for updates

Pulsed laser-patterned high-entropy single-atomic sites and alloy coordinated graphene oxide for pH-universal water electrolysis†

Yeryeong Lee,‡[a] Jayaraman Theerthagiri,‡[a] Wanwisa Limphirat,‡[b] Ganga Periyasamy,[c] Gyoung Hwa Jeong,[d] Soorathep Kheawhom, [ID] *[e] Yongbing Tang [ID] [f] and Myong Yong Choi [ID] *[ag]

Synthesizing catalysts with multiple single-metal atoms remains challenging. Here, we introduce high-entropy single-atom catalysts (HESACs) co-coordinated with six elements from a FeRuPtNiCoPd high-entropy alloy (HEA) on graphene oxide supports (HESAC–HEA/GO) *via* single-pot pulsed laser irradiation in liquids (PLIL). This method leverages tailored surface composition and diverse active sites for electrochemical overall water splitting (OWS) across a wide pH range. The synergistic interactions in high-entropy systems and rapid photoreduction of Fe^{2+} *via* PLIL enhance nuclei generation and active sites compared to Fe^{3+}, achieving high hydrogen evolution reaction in 0.5 M H_2SO_4 with η of 49 mV at 10 mA cm^{-2}, and record-high oxygen evolution reaction in 1.0 M KOH with η of 398 mV. Optimized HESAC–HEA/GO–Fe^{2+} shows exceptional OWS performance with lower cell voltage compared to HESACC–HEA/GO–Fe^{3+} and Pt/C. This study offers a robust pathway for fabricating versatile catalysts and facilitates mechanistic insights through *in situ* Raman and density functional theory analyses.

1. Introduction

Hydrogen (H_2) produced *via* water electrolysis represents a revolutionary step forward as a clean energy carrier and is considered a potential replacement for fossil fuels due to its zero CO_2 emissions and high energy density. The hydrogen evolution reaction (HER) plays a crucial role in electrocatalytic overall water splitting (OWS) for H_2 generation fuel.[1–6] Various water electrolysis systems operate under different pH conditions, necessitating tailored electrolyte environments; for instance, seawater electrolysis occurs in neutral solutions, proton exchange membrane electrolyzers require strongly acidic conditions, and commercial alkaline electrolyzers function in strongly basic media. Therefore, the development of pH-universal catalysts capable of efficiently facilitating HER under both acidic and alkaline conditions remains a formidable challenge. Despite ongoing research, such electrocatalysts are largely inaccessible.[7–14] Although significant progress has been made in the design of novel catalysts, state-of-the-art materials for HER still rely heavily on precious metals, such as Pt, as well as RuO_2 and IrO_2 for the oxygen evolution reaction (OER). Consequently, the development of cost-effective and highly efficient non-noble metal-based catalysts has emerged as a key research focus.

Recently, high-entropy alloys (HEAs) have gained significant attention due to their unique physicochemical properties arising from their multicomponent nature, which enables remarkable electrocatalytic performance through compositional tuning, lattice distortion, electronic structure modulation, and cocktail effects.[15–17] The disordered atomic arrangement in HEAs grants them more appealing properties compared with conventional alloys and single-element catalysts, making HEAs theoretically ideal candidates for versatile electrocatalysts effective in HER and OER. Generally, the performance of any catalysts is largely dependent on the reactant's adsorption onto the catalyst active sites. The distinctive benefit of HEAs is the presence of diverse metal sites within catalytic materials. The remarkable performance and stability of HEA materials are attributed to the synergistic activity of

[a]Department of Chemistry (BK21 FOUR), Research Institute of Natural Sciences, Gyeongsang National University, Jinju 52828, Republic of Korea. E-mail: mychoi@gnu.ac.kr

[b]Beamline Division, Synchrotron Light Research Institute (SLRI), Nakhon Ratchasima, 30000, Thailand

[c]Department of Chemistry, Bangalore University, Jnana Bharathi Campus, Bangalore 560056, India

[d]Research Institute for Green Energy Convergence Technology, Gyeongsang National University, Jinju, 52828, Republic of Korea

[e]Department of Chemical Engineering, Faculty of Engineering, Chulalongkorn University, Bangkok, 10330, Thailand. E-mail: soorathep.k@chula.ac.th

[f]Advanced Energy Storage Technology Research Center, Shenzhen Institutes of Advanced Technology, Chinese Academy of Sciences, Shenzhen 518055, China

[g]Core-Facility Center for Photochemistry & Nanomaterials, Gyeongsang National University, Jinju 52828, Republic of Korea

† Electronic supplementary information (ESI) available. See DOI: https://doi.org/10.1039/d5ta00117j

‡ These authors contributed equally to this work.

This journal is © The Royal Society of Chemistry 2025

J. Mater. Chem. A, 2025, **13**, 9073–9087 | **9073**

these multiple metal sites. However, the simultaneous existence of numerous challenging adsorption sites on HEA often results in insufficient electrochemical reaction selectivity. The prospective enhancement in catalytic effectiveness is anticipated through the careful directive of the interaction among reactant and catalyst active centers, aiming for competitive preferential adsorption of reactive species.[18,19]

In response to this, single-atom catalysts (SACs) have gained widespread recognition as cutting-edge materials and have emerged as a booming field in various industrial reactions owing to their unique geometric structure and utilization of maximum atomic sites.[20,21] The simplicity of SACs is their strength and weakness; while they offer unparalleled atom utilization of SAC, they also severely restrict active site tailoring and their applicability across a broad range of catalytic HER/OER reactions. Recognizing the limitations of SAC modification, researchers have explored dual or binary SACs. These novel catalysts exhibit superior performance compared with their individual SAC counterparts owing to synergistic effects of multiple-single atoms, wherein the activity of the primary SAC is modulated by the presence of an additional single-metal atom.[22,23] Various synthesis techniques, including pyrolysis,[24] high-temperature migration,[25] atomic layer deposition,[26] and wet chemical methods,[27] have been explored for the production of SACs. In addition, while numerous studies have concentrated on exploring the active sites and mechanisms of nanocatalysts and SACs towards HER/OER, the equally crucial catalyst system of HEA catalysts has been largely overlooked in terms of accurately identifying active centers and understanding their activity origins.

Herein, we synthesize multiple metallic SACs with six distinct elements—FeRuPtNiCoPd (referred to as high-entropy single-atom catalysts, HESACs)—alongside FeRuPtNiCoPd HEA alloy co-coordinated on graphene oxide (GO) supports *via* photoreduction methods by employing pulsed laser irradiation in liquids (PLIL). This approach transfers various metal components to single-phase HEA. Interestingly, final products exhibit typical features of the HESACs and HEA of FeRuPtNiCoPd co-coordinated on GO supports, which resulted from the photoreduction process (refer to Results and discussion "formation mechanism"). The use of GO as support enhances dispersion, provides a high surface area, and facilitates efficient electron transfer during catalytic reactions. This combination of the HESACs and HEA on GO supports creates a versatile and robust platform that can catalyze electrochemical HER, OER, and OWS reactions of a diverse pH range, making it promising for various industrial and research applications.

2. Experimental

2.1 Synthesis of HESACs and HEA on GO support

The multiple single-atom and FeRuPtNiCoPd HEA co-coordinated GO support (HESAC–HEA/GO) was produced with a facile single-pot PLIL technique. Initially, a commercially purchased 1 wt% GO solution was diluted to 0.1 wt% using deionized water under ultrasonic treatment for 10 min.

Separately, a metal salt solution was prepared in dimethylformamide (DMF) with the following concentrations: 30 mM for Pt^{2+} (K_2PtCl_4), Pd^{2+} (K_2PdCl_4), and Ru^{3+} ($RuCl_3 \cdot xH_2O$) and 15 mM for Ni^{2+} ($NiCl_2 \cdot 6H_2O$), Co^{2+} ($CoCl_2 \cdot 6H_2O$), and Fe^{2+} ($FeCl_2 \cdot 6H_2O$) or Fe^{3+} ($FeCl_3 \cdot 6H_2O$). Subsequently, 50 μL of each metal salt solution was added to 200 μL of the 0.1 wt% GO solution. The resulting mixture was then subjected to irradiation using a non-focused Nd:YAG pulsed laser beam with a wavelength of 1064 nm and a fluence of 200 mJ (Surelite II-10, 10 Hz, 10 ns) for 10 min. During the PLIL process, metal salts were reduced to their metallic states in DMF *via* a photothermal mechanism, where the solvent functioned both as a reducing agent and as a stabilizing medium. This approach enables the simultaneous synthesis of HEAs while ensuring the uniform distribution and stabilization of single atoms, both of which are critical for catalytic performance. Under high-energy laser irradiation, DMF undergoes thermal decomposition, generating reactive radicals, including formyl (˙HCO), methyl (˙CH_3), amino (˙NH_2), and hydrogen (˙H) radicals, which participate in reduction reactions by transferring electrons to metal ions. Successively, the obtained HESAC–HEA/GO precipitate was separated using ~14 000 rpm centrifugation for 5 min, rinsed four times with methanol and water, and then subjected to air drying under ambient conditions for 12 h. Depending on the type of iron salt source, it was termed HESAC–HEA/GO–Fe^{2+} when using iron(ɪɪ) chloride tetrahydrate and HESAC–HEA/GO–Fe^{3+} when using iron(ɪɪɪ) chloride hexahydrate.

Detailed Experimental section: materials; characterization techniques; electrochemical analyses; *in situ/operando* electrochemical Raman probe studies; X-ray absorption (XAS) studies; computational study; ESI Fig. S1 to S32 and Tables S1 to S3 are provided in ESI files.†

3. Results and discussion

3.1 Structural analyses

The synthesis pathways for the HESACs and FeRuPtNiCoPd HEA-coordinated GO support (HESAC–HEA/GO) *via* the PLIL route are shown in Fig. 1a and S1.† Herein, we attempted to develop new tandem catalysts under a facile and green strategy, capitalizing on the inherent physicochemical properties of pure GO, including hydrophilicity, high conductivity, and large specific surface area, all without artificially transforming GO into reduced GO. The XRD pattern of GO correlate with those of previous reports, showing a strong XRD signal at a 2θ value of 11.3° corresponding to the (002) plane of GO (Fig. 1b(i)), indicative of interlayer spacing caused by the existence of O-comprising functional groups in GO structure.[28] The PLIL process was used to selectively reduce metal ions (Fe^{2+} or Fe^{3+}, Ru^{3+}, Pt^{2+}, Ni^{2+}, Co^{2+}, and Pd^{2+}) for the simultaneous formation of corresponding single atoms and HEAs on the GO support. Thus, the formation of FeRuPtNiCoPd HEA and HESACs through the PLIL process relies predominantly on the optically induced solvents decomposition, occurring without the need for other reducing agents. Nevertheless, solvents exposed to laser irradiation produce $CH_3^•$, solvated electrons, and ˙H radicals, serving as potent reducing agents in the liquids to

9074 | *J. Mater. Chem. A*, 2025, **13**, 9073–9087

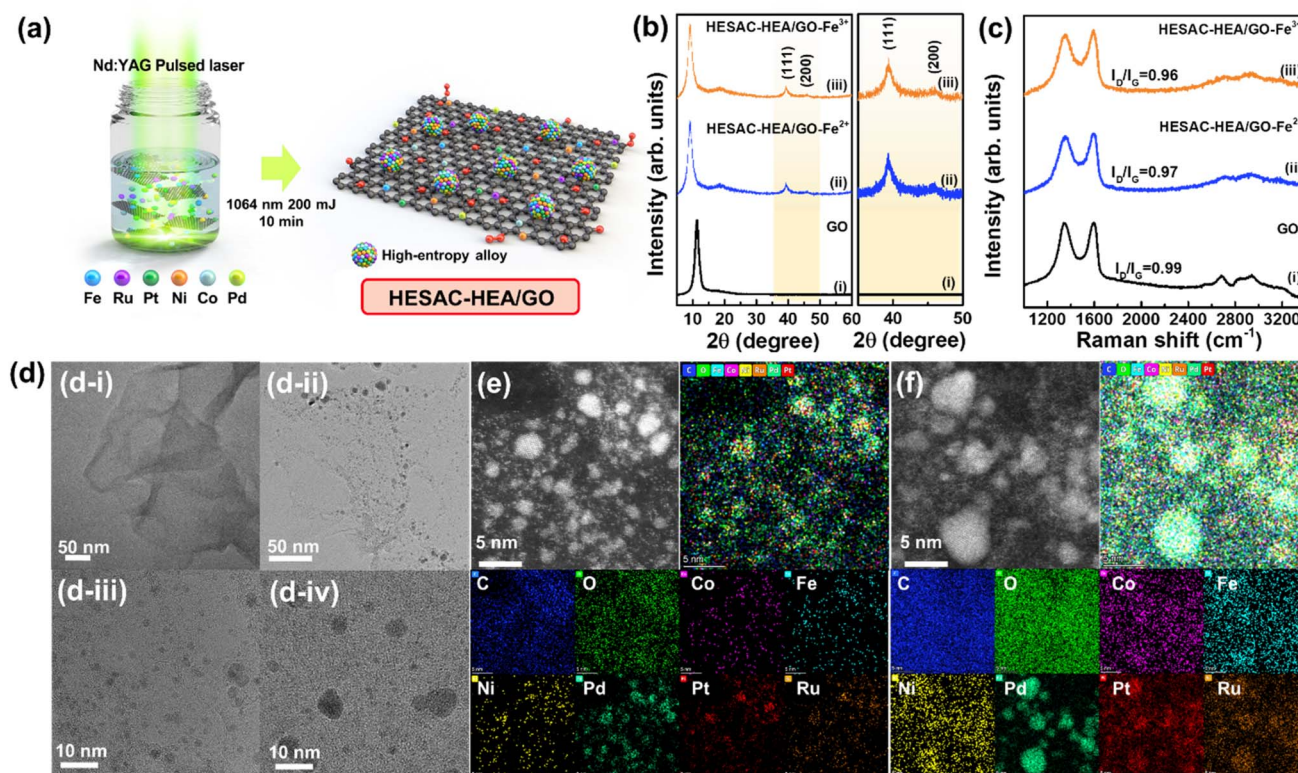This journal is © The Royal Society of Chemistry 2025

Fig. 1 (a) Graphic of the PLIL synthesis of HESACs−HEA/GO. (b) XRD and (c) Raman graphs of (i) pure GO, (ii) HESAC−HEA/GO−Fe²⁺, and (iii) HESAC−HEA/GO−Fe³⁺. (d) HRTEM images: (d-i) pure GO, (d-ii & d-iii) low and high magnification HESAC−HEA/GO−Fe²⁺, and (d-iv) HESAC−HEA/GO−Fe³⁺. (e and f) HAADF-STEM and STEM elemental mapping of HESAC−HEA/GO−Fe²⁺ and HESAC−HEA/GO−Fe³⁺.

simultaneously reduce the metal salts into corresponding metals.[29–32] As observed from the XRD pattern (Fig. 1b(ii and iii)), the HEAs were synthesized, where six elements, namely Fe (JCPDS: 06-0696), Ru (JCPDS: 88-2333), Pt (JCPDS: 04-0802), Ni (JCPDS: 04-0850), Co (JCPDS: 15-0860), and Pd (JCPDS: 05-0681), form single fcc phase diffraction at peaks $2\theta = 39.3°$ and $45.9°$, consistent to the (111) and (200) planes of HEA, along with the peak of GO. A weak HEA peak was detected in the XRD of HESAC−HEA/GO−Fe²⁺ (Fig. 1b(ii)) and HESAC−HEA/GO−Fe³⁺ (Fig. 1b(iii)), owing to the less HEA content on the GO nanosheets surface. The presence of minor peaks persisting at a 2θ value of 18.5° suggests that GO is not completely bonded or interconnected with oxygen atoms (Fig. 1b(ii and iii)).[33]

The crystalline size (D) and lattice strain (ε) of the synthesized HESAC−HEA/GO−Fe²⁺ ($D \approx 4.7$ nm; $\varepsilon \approx 0.021\%$) and HESAC−HEA/GO−Fe³⁺ ($D \sim 5.0$ nm; $\varepsilon \sim 0.020\%$) were assessed using the Scherrer's and Williamson–Hall formulas. Thus, the crystalline parameters revealed that the HESAC−HEA/GO−Fe²⁺ sample exhibited a smaller crystalline size and higher lattice strain, suggesting that it possesses more catalytically active surface sites than HESAC−HEA/GO−Fe³⁺, resulting in improved electrochemical applications.[34] The controlled crystalline growth of HESAC−HEA/GO−Fe²⁺ particles may be attributed to the easier laser reduction of Fe²⁺ to Fe than the reduction of Fe³⁺ to Fe⁰. Fe³⁺ has a higher oxidation state than Fe²⁺, making its reduction reactions more challenging. The additional electron required for reduction is more readily available in Fe²⁺ than in

Fe³⁺, thereby facilitating the reduction process. This was confirmed by ICP-OES analysis, which revealed a higher Fe content in HESAC−HEA/GO−Fe²⁺ compared to HESAC−HEA/GO−Fe³⁺ (Table S1†). Furthermore, the ratios of noble metals for instance Pt, Pd, and Ru were lower in HESAC−HEA/GO−Fe²⁺, which was attributed to the lower reduction potential of Fe²⁺ than that of Fe³⁺. During coreduction, the availability of electrons for the reduction of Pd²⁺, Pt²⁺, and Ru³⁺ may be limited when using Fe²⁺ salt, leading to the lower reduction content of these metal ions in the HEA. Additionally, the lower content of Pd, Pt, and Ru in the HEA over Co, Fe, and Ni can be attributed to their larger atomic size, hindering their diffusion rate during the alloying process (Table S1†).[35] Consequently, the reduced noble metal content in HESAC−HEA/GO−Fe²⁺ decreases production costs and increases the scalability of catalyst for practical utility.

The Raman spectra of the produced pure GO, HESAC−HEA/GO−Fe²⁺, and HESAC−HEA/GO−Fe³⁺ are revealed in Fig. 1c. The Raman typical signals were detected for all samples at 1344–1350, 1594–1696, 2686–2720, and ~2943 cm⁻¹, which were allotted to D, G, 2D, and D + G bands, correspondingly. The D to G-band (I_D/I_G) signal intensity ratio for pure GO, HESAC−HEA/GO−Fe²⁺, and HESAC−HEA/GO−Fe³⁺ was 0.99, 0.97, and 0.96, correspondingly. This intensity ratio serves as an indicator of the degree of graphitic ordering, with low values suggesting increased graphitic ordering and few defects. Notably, the I_D/I_G values for the initially received pure GO as well as synthesized

HESAC–HEA/GO–Fe^{2+} and HESAC–HEA/GO–Fe^{3+} samples were nearly identical, considering uncertainty measurements. This suggests that Raman spectra show no remarkable difference in the degree of disorder for GO before and after the fabrication of HESAC–HEA composites on the GO support during the PLIL synthesis process.

The UV-vis spectra of GO and HESAC-HEA-Fe^{2+}/GO are shown in Fig. S2.† Both samples exhibit the two characteristic peaks of GO: a shoulder peak around ~310 nm associated with the plasmon peak of the n–π* transition from C=O, and another peak at ~240 nm related to the plasmon peak caused by the π–π* transition in C=C of GO.[36] The extended visible light absorption of HESAC–HEA/GO can be attributed to the presence of patterned noble metallic nanostructures (Ru, Pt, Pd) on GO, which enhance light absorption in the visible region through surface plasmon resonances.[37] Furthermore, FTIR spectral analysis was employed to investigate the nature of chemical bonding among the metals in HESAC–HEA with GO. The spectra of GO and HESAC–HEA/GO exhibit a broad band at 3000–3500 cm^{-1}, attributed to the O–H vibrational mode of C–OH from GO, and another band at 1049 cm^{-1} assigned to C–O stretching vibrations (Fig. S3†). Several characteristic peaks corresponding to various functionalities are also observed and indexed in the spectrum.[38,39] The lack of significant changes in the HESAC–HEA/GO spectra suggests that the interactions between the metals in HESAC–HEA and GO are subtle and that the low metal concentration limits FTIR's ability to detect minor changes.

HRTEM images of pure GO, HESAC–HEA/GO–Fe^{2+}, and HESAC–HEA/GO–Fe^{3+} are exposed in Fig. 1d(i to iv). As depicted in Fig. 1d(i), the HRTEM image of pure GO reveals a nanosheet-like morphology. In Fig. 1d(ii–iv), the HRTEM images of HESAC–HEA/GO–Fe^{2+} and HESAC–HEA/GO–Fe^{3+} demonstrate that the HESACs and FeRuPtNiCoPd HEA are highly disordered yet well anchored on the GO supports. Furthermore, the atomic dispersion of multiple metal atoms (Fe, Ru, Pt, Ni, Co, and Pd) along with the spherical HEA alloy particles co-coordinated on GO supports is clearly observed in the HAADF-STEM and STEM mapping pictures (Fig. 1(e and f) and S4†). Besides the metal atoms, the mapping images display an evenly distribution of the C and O across the entire GO supports. These results offer compelling evidence for the effectiveness of the proposed synthesis strategy in successfully producing HESACs and HEA ranging up to undecimal compositions on GO supports via a one-pot PLIL process. Additionally, the presence of the fcc-structured HEA was confirmed by the lattice planes observed in the HRTEM image of the HESAC–HEA/GO–Fe^{2+} sample, which corresponds well with the XRD analysis (Fig. S5†). In addition, the FESEM images of HESAC–HEA/GO–Fe^{2+} and HESAC–HEA/GO–Fe^{3+} support the uniform distribution of HESAC–HEA on the GO nanosheet support, as displayed in Fig. S6a and S6b.† The elemental composition of the synthesized samples characterized via FESEM–EDS mapping measurement confirms the existence of six metals along with C and O in the HESAC–HEA/GO–Fe^{2+} and HESAC–HEA/GO–Fe^{3+} samples, aligning well with the XRD and ICP-OES observations (Fig. S6a and S6b†). For a clearer understanding of the role of

the PLIL process, we attempted the synthesis using the reaction mixture of metal salts with GO without applying laser irradiation. However, we observed only the presence of GO, with no evidence of metal salt reduction, as confirmed by XRD (Fig. S7†) and FESEM-EDS analyses (Fig. S8†).

XPS studies were employed to recognize the electronic structure, elemental configurations, and surface valence states of the pure GO and synthesized HESAC–HEA/GO samples. The XPS spectra of pure GO are depicted in Fig. S9.† The wide-scan XPS spectra of pure GO showed the occurrence of C and O (Fig. S9a†). The high-resolution C 1s spectra of GO shown in Fig. S9b† could be resolved into five peaks, inferring the existence of carbon, with signals at the binding energies (BEs) of ~284.2 and 285.3 eV showing the presence of C sp^2 and C sp^3, respectively, and peaks at 286.1, 287.2, and 288.9 eV displaying the presence of carbon in C–OH, C=O, and COOH bonds, respectively. Fig. S9c† shows O 1s spectra being split into three signals corresponding to C=O, C–O–H, and COOH bonds at 531.3, 533.1, and 534.6 eV, respectively.[28,40,41] The XPS spectra of the HESAC–HEA/GO–Fe^{2+} and HESAC–HEA/GO–Fe^{3+} materials are revealed in Fig. 2 and S10,† correspondingly. The wide-scan XPS spectra of HESAC–HEA/GO–Fe^{2+} (Fig. 2a) and HESAC–HEA/GO–Fe^{3+} (Fig. S10a†) exhibited signals corresponding to C, O, Co, Fe, Ni, Pt, Pd, and Ru. As shown in Fig. 2b, c, S10b and S10c,† the C 1s and O 1s core-level spectra of HESAC–HEA/GO–Fe^{2+} and HESAC–HEA/GO–Fe^{3+} maintained similar XPS peaks and chemical states as those observed in the pure GO nanosheet (Fig. S9†). This confirms that the synthesized HESAC–HEA/GO–Fe^{2+} and HESAC–HEA/GO–Fe^{3+} samples retain the structural properties of GO, as evidenced by the XRD patterns and Raman spectra discussed above.

The XPS spectra of HESAC–HEA/GO–Fe^{2+} (Fig. 2d–i) and HESAC–HEA/GO–Fe^{3+} (Fig. S10d–i†) synthesized via PLIL show additional signals corresponding to metallic Co, Fe, Ni, Pt, Pd, and Ru at low BE values (Co^0 at 779.0 eV, Fe^0 at 709.2 eV, Ni^0 at 852.5 eV, Pt^0 at 71.1 eV, Pd^0 at 335.5 eV, and Ru^0 at 459.5 eV). Furthermore, the XPS spectra of HESAC–HEA/GO–Fe^{2+} and HESAC–HEA/GO–Fe^{3+} samples exhibited the coexistence of target zero-valent metal peaks, with peaks originating from inevitable surface-bound native oxides in the prepared samples. Owing to the surface sensitivity of XPS, strong oxide signals tend to dominate metal signals.

Fig. 2d illustrates the Co 2p graph, which is resolved into two pairs of Co $2p_{3/2}$ and Co $2p_{1/2}$ doublets, along with their satellite signals. The signals observed at 780.5 and 795.8 eV are attributed to Co^{3+}, while those appearing at 782.7 and 798.1 eV are assigned to Co^{2+}.[42,43] In Fig. 2e, the Fe 2p graph reveals two pairs of Fe $2p_{3/2}$ and Fe $2p_{1/2}$ doublets where the signals located at 710.9 and 723.6 eV are related with Fe^{2+}, while those observed at 713.0 and 726.0 eV are accredited to Fe^{3+}.[44] The Ni 2p shown in Fig. 2f reveal four bands where Ni^{2+} $2p_{3/2}$ and $2p_{1/2}$ raise at 855.7 and 873.8 eV, while Ni^{3+} $2p_{3/2}$ and $2p_{1/2}$ emerge at 860.1 and 878.8 eV.[45] Fig. 2g displays the Pt 4f core-level spectra, where the 71.1 and 74.5 eV peaks are accredited to Pt^0 $4f_{7/2}$ and Pt^0 $4f_{5/2}$, correspondingly, while the 72.8 and 76.1 eV peaks can be attributed to Pt^{2+} $4f_{7/2}$ and Pt^{2+} $4f_{5/2}$, and the 73.8 and 77.1 eV peaks represent Pt^{4+} $4f_{7/2}$ and Pt^{4+} $4f_{5/2}$, correspondingly. The Pd

9076 | *J. Mater. Chem. A*, 2025, **13**, 9073–9087

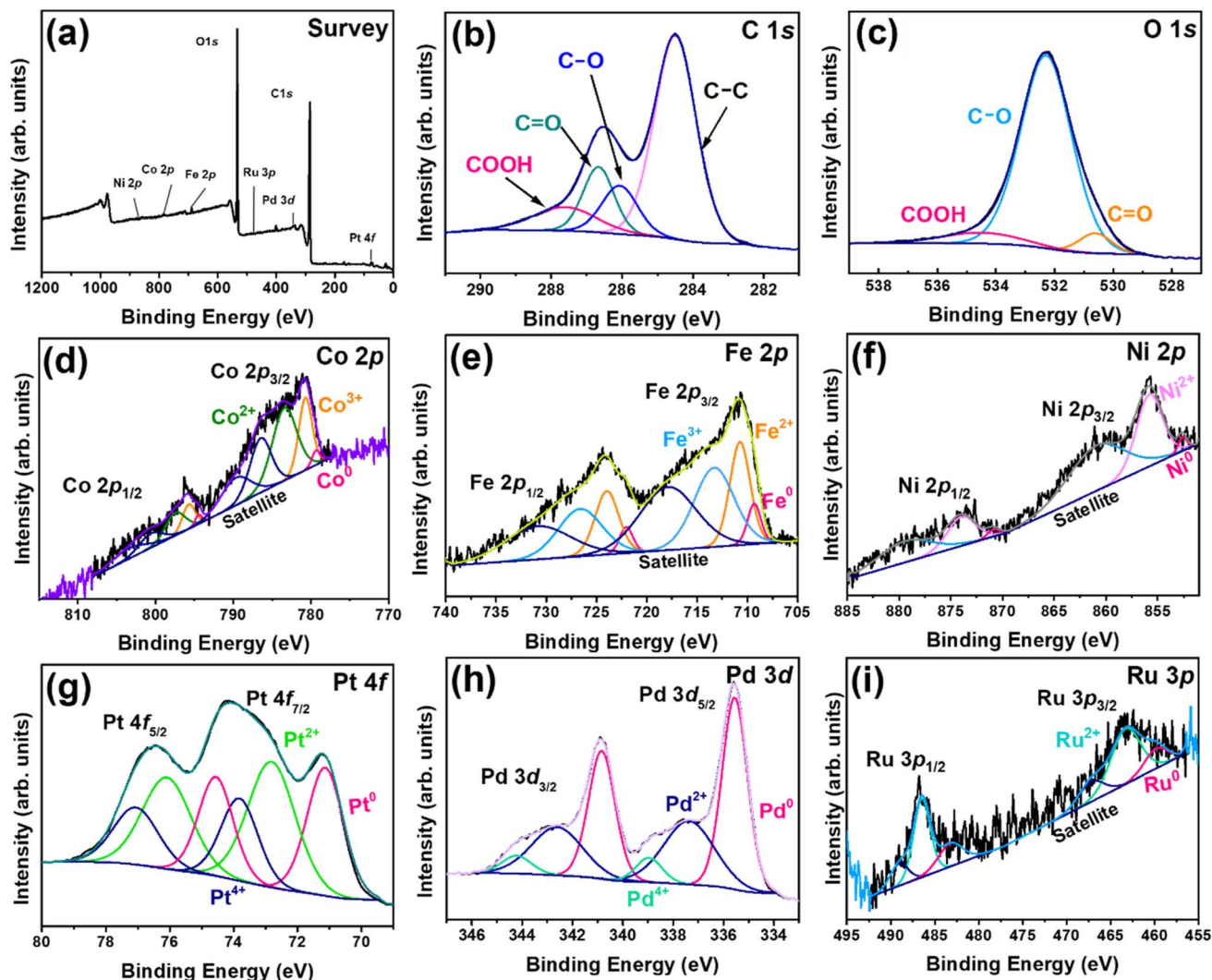This journal is © The Royal Society of Chemistry 2025

Fig. 2 XPS spectra of the HESAC–HEA/GO–Fe^{2+}: (a) full-survey, (b) C 1s, (c) O 1s, (d) Co 2p, (e) Fe 2p, (f) Ni 2p, (g) Pt 4f, (h) Pd 3d, and (i) Ru 3p.

3d spectra shown in Fig. 2h exhibit the BEs of Pd^0 3d$_{5/2}$, Pd^0 3d$_{3/2}$, Pd^{2+} 3d$_{5/2}$, Pd^{2+} 3d$_{3/2}$, Pd^{4+} 3d$_{5/2}$, and Pd^{4+} 3d$_{3/2}$ at 335.5, 340.8, 337.3, 342.7, 339.0, and 344.2 eV, correspondingly. The Ru 3p spectrum shown in Fig. 2i illustrates the presence of metallic Ru, with peaks observed at 459.4 and 483.0 eV corresponding to Ru^0 3p$_{3/2}$ and Ru^0 3p$_{1/2}$, correspondingly. Two other peaks positioned at 463.1 and 886.5 eV are ascribed to Ru^{2+} 3p$_{3/2}$ and Ru^{2+} 3p$_{1/2}$, correspondingly. Fig. S10(d–i)† displays the high-resolution spectra of the HESAC–HEA/GO–Fe^{3+} sample, revealing a similar trend to that of the HESAC–HEA/GO–Fe^{2+} sample.

In addition to XPS analysis, the chemical state, electronic structure, and coordination situation of the produced HESA-HEA on GO support (HESAC–HEA/GO–Fe^{2+}) was determined at the atomic level using XANES and extended EXAFS spectra. The obtained XANES and EXAFS results in K or L-edge and R space for the high entropy material (FeRuPtNiCoPd) and the standard materials are presented in Fig. 3. From Fig. 3, it can be detected that the K-edge absorption energies of Fe, Co, and Ni (Fig. 3a–c), as well as the L-edge absorption energies of Ru, Pd,

and Pt elements (Fig. 3d–f), are all present in between those of the standard materials (metal and metal oxides). This suggests that the local atomic environment surrounding these elements differs from their corresponding bulk metals and indicates that the oxidation states of each element are higher than those of the bulk metals. From these results, it can be contingent that the Fe, Co, Ni, Ru, Pd, and Pt elements are atomically dispersed within the GO sheet and their atomic centers coordinated with oxygen atoms to form M–O bonds (Fe–O, Co–O, Ni–O, Pd–O, Ru–O, and Pt–O) through interaction with O-functional groups in the GO support. Furthermore, Fig. 3g–j displays the Fourier-transformed EXAFS graphs (in R space) at the Fe, Co, Ni K-edges and Pt L-edge, highlighting the distinct local atomic environments across the samples. However, measurements of the Pd and Ru element EXAFS spectra were not feasible due to their similar energy levels of L (I, III and III) shell. The dominant peak observed for all six elements is attributed to the metal-oxide coordination shell.[22,46] Hence, it is evident that each of the six elements has been melted and remains as single isolated atoms coordinated with O (forming Fe–O–C, Co–O–C, Ni–O–C, and Pt–
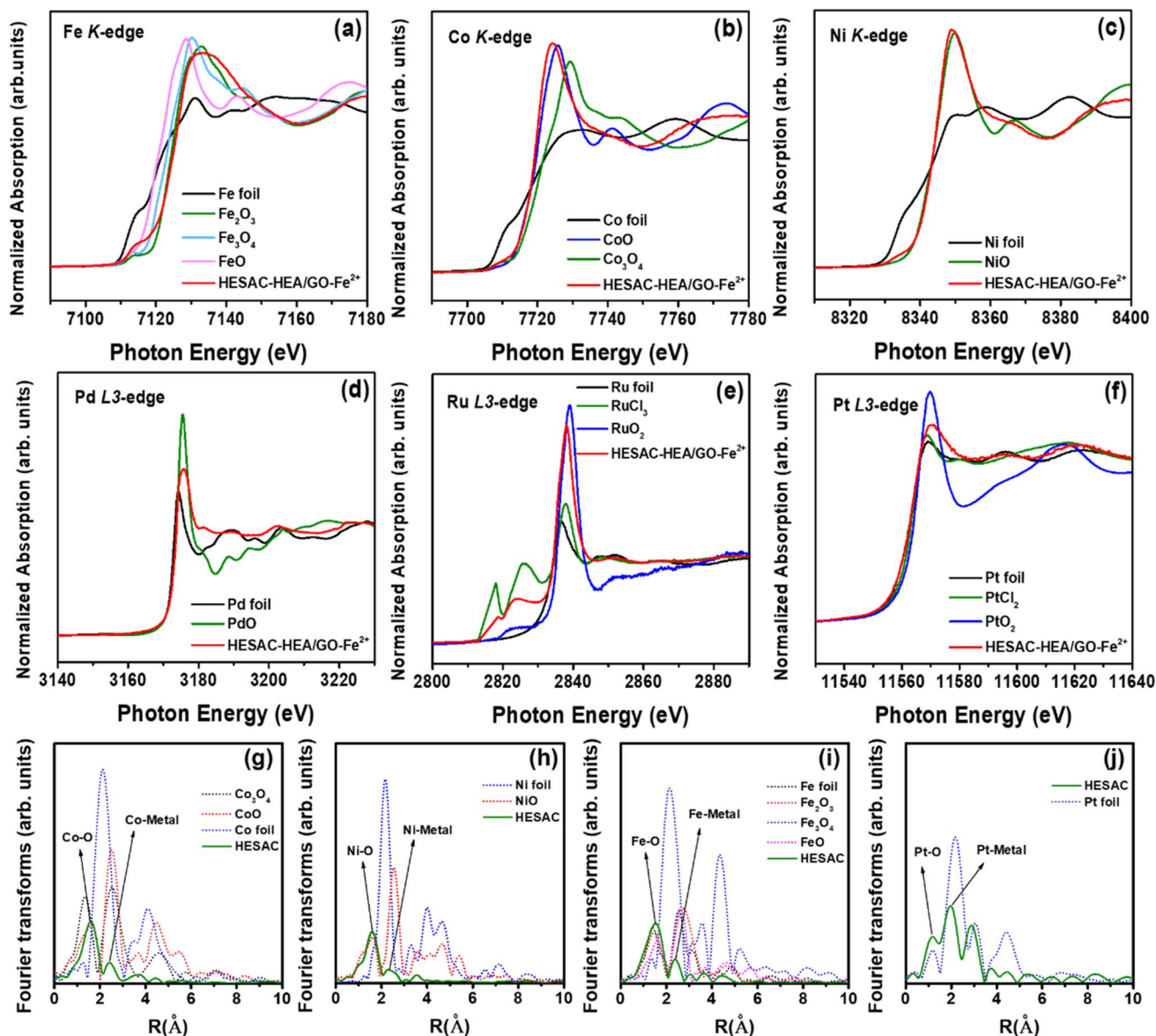
Fig. 3 XAS analysis of HESAC–HEA/GO–Fe^{2+} sample: (a–f) XANES graphs of the Fe K-edge, Co K-edge, and Ni K-edge, (a–c) Pd L_3-edge, Ru L_3-edge, and Pt L_3-edge, (g–j) EXAFS graphs in R space of Co, Ni, Fe, and Pt for HESAC–HEA/GO–Fe^{2+} sample (HESAC refers to HESAC–HEA/GO–Fe^{2+}).

O–C electron conjugated complexes) within the GO structure.[47] In addition to the prevalence of M–O species, a few signals indicating metal–metal interactions within the transition layer are also detected from the EXAFS results, which may be accredited to the formation of a HEA (Fig. 3g–j). These observations suggest the formation of both isolated single atoms and an fcc phase of metallic HEA on GO. Collectively, the XANES and EXAFS spectra provide comprehensive insights into the oxidation state and local atomic environment, correlating with the information obtained from XPS analysis.

3.2 Electrochemical HER

The effectiveness of multielement HESAC–HEA/GO–Fe^{2+} and HESAC–HEA/GO–Fe^{3+} as electrocatalysts for HER was examined using a usual three-electrode arrangement across a wide pH

range using three different electrolytes: 1.0 M KOH, 0.5 M H_2SO_4, and 0.1 M $KClO_4$. Fig. 4a depicts the HER graphs of the HESAC–HEA/GO–Fe^{2+} and HESAC–HEA/GO–Fe^{3+} electrocatalysts in these three different electrolytes. In 0.5 M H_2SO_4, the HESAC–HEA/GO–Fe^{2+} catalyst displayed superior HER function with an η of 49 and 155 mV at current densities (J) of 10 and 50 mA cm^{-2}, correspondingly; notably, these values are inferior than the HESAC–HEA/GO–Fe^{3+} catalyst (115 and 283 mV at 10 and 50 mA cm^{-2}, correspondingly) and comparable with commercial Pt/C catalyst, as represented in Fig. 4b and S11.† The HER of the HESAC–HEA/GO–Fe^{2+} and HESAC–HEA/GO–Fe^{3+} electrocatalysts in the 1.0 M KOH and 0.1 M $KClO_4$ electrolytes was inferior than that in 0.5 M H_2SO_4, as exposed in Fig. 4a and b. The variation in electrocatalytic HER activity HESAC–HEA/GO–Fe^{2+} and HESAC–HEA/GO–Fe^{3+} samples
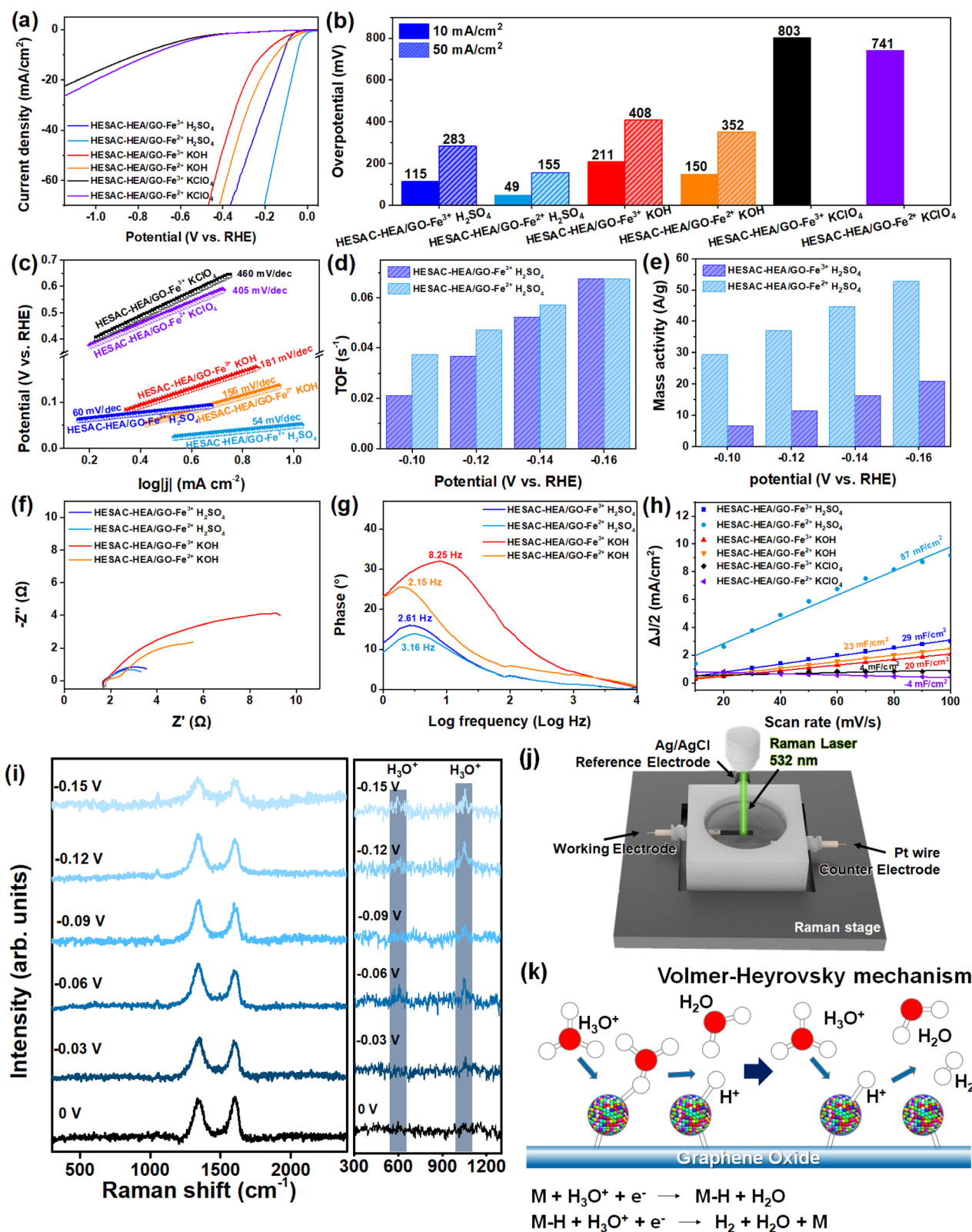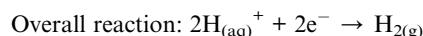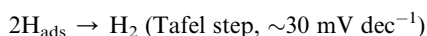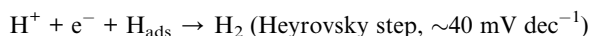
9078 | *J. Mater. Chem. A*, 2025, **13**, 9073–9087

This journal is © The Royal Society of Chemistry 2025

Fig. 4 (a) HER polarization graphs of HESAC−HEA/GO−Fe^{2+} and HESAC−HEA/GO−Fe^{3+} in 0.5 M H$_2$SO$_4$, 1.0 M KOH, and 0.1 M KClO$_4$ solutions at 5 mV s^{-1}, (b) η at 10 and 50 mA cm^{-2}, (c) Tafel slope, (d) TOF, (e) mass activity, (f and g) Nyquist and Bode plots, (h) C_{dl} plot, (i) *in situ* Raman spectra of the HESAC−HEA/GO−Fe^{2+} electrocatalyst in 0.5 M H$_2$SO$_4$ during HER process under different potentials, (j) schematic of the *in situ* electrochemical Raman setup, and (k) proposed HER pathway over the HESAC−HEA/GO−Fe^{2+} electrocatalyst.
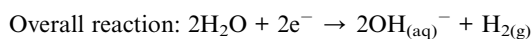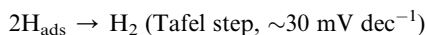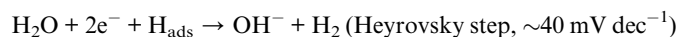
This journal is © The Royal Society of Chemistry 2025

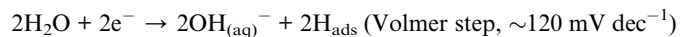*J. Mater. Chem. A*, 2025, **13**, 9073–9087 | **9079**

across different electrolytes, such as 0.5 M H_2SO_4, 1.0 M KOH, and 0.1 M $KClO_4$, can be primarily attributed to the pH level of the electrolyte, which plays a crucial role in electrocatalytic HER activity. Acidic H_2SO_4 promotes HER activity owing to its increased proton concentration, facilitating the establishment of crucial H* intermediates. In contrast, the higher concentration of hydroxide ions in basic solutions such as KOH may interfere with HER kinetics or promote the formation of stable hydroxyl intermediates instead of H*. Additionally, other ions present in the electrolyte, such as K^+ and ClO_4^-, can compete with H^+ or OH^- for adsorption sites on the catalyst surface, thereby reducing HER kinetics. Furthermore, the Tafel slope derived from polarization curves revealed that HESAC–HEA/GO–Fe^{2+} substantially promoted HER kinetics, demonstrating a lower Tafel slope of 54, 156, and 405 mV dec^{-1} in 0.5 M H_2SO_4, 1.0 M KOH, and 0.1 M $KClO_4$, correspondingly, than HESAC–HEA/GO–Fe^{3+} (60, 181, 460 mV dec^{-1}, respectively), as shown in Fig. 4c. Notably, HESAC–HEA/GO–Fe^{2+} exhibited superior HER activity, whereas HESAC–HEA/GO–Fe^{3+} demonstrated relatively limited performance (Fig. S12†). This enhanced activity is likely attributed to the smaller crystalline and particle sizes of HESAC–HEA/GO–Fe^{2+}, which provide a larger number of accessible active sites for HER. The formation of smaller particles can be attributed to the faster reduction of Fe^{2+} to Fe^0 compared to Fe^{3+} to Fe^0, owing to the lower oxidation state of Fe^{2+}. A slower reduction rate leads to the formation of fewer nuclei, which subsequently aggregate to form larger particles, thereby reducing the availability of active sites.

The proposed reaction pathway and rate-determining steps (RDS) participated in the HER process were inferred from the Tafel slope values following previous reports.[48,49] The reaction steps remain consistent in basic and neutral media, but they deviate in acidic electrolytes, as described below:

In acidic electrolytes,

$$H^+ + e^- \rightarrow H_{ads} \text{ (Volmer step, } \sim120 \text{ mV dec}^{-1})$$

$$H^+ + e^- + H_{ads} \rightarrow H_2 \text{ (Heyrovsky step, } \sim40 \text{ mV dec}^{-1})$$

$$2H_{ads} \rightarrow H_2 \text{ (Tafel step, } \sim30 \text{ mV dec}^{-1})$$

$$\text{Overall reaction: } 2H_{(aq)}^+ + 2e^- \rightarrow H_{2(g)}$$

In alkaline/neutral electrolytes,

$$2H_2O + 2e^- \rightarrow 2OH_{(aq)}^- + 2H_{ads} \text{ (Volmer step, } \sim120 \text{ mV dec}^{-1})$$

$$H_2O + 2e^- + H_{ads} \rightarrow OH^- + H_2 \text{ (Heyrovsky step, } \sim40 \text{ mV dec}^{-1})$$

$$2H_{ads} \rightarrow H_2 \text{ (Tafel step, } \sim30 \text{ mV dec}^{-1})$$

$$\text{Overall reaction: } 2H_2O + 2e^- \rightarrow 2OH_{(aq)}^- + H_{2(g)}$$

The Tafel step represents a chemical desorption process common to all electrolytes. The Volmer step initiates with the H_2O splitting and involves the subsequent of hydrogen atoms

adsorption on the active surface sites of the electrocatalyst/electrode. Then, H_2 gas evolves through an electrochemical process identified as the Heyrovsky step or *via* a chemical desorption process termed the Tafel step. Based on this framework, the HER mechanism involves two mechanistic pathways: Volmer–Heyrovsky and Volmer–Tafel reaction pathways, with Volmer serving as the initial adsorption step in both mechanisms. The Tafel slopes of HESAC–HEA/GO–Fe^{2+} and HESAC–HEA/GO–Fe^{3+} in acidic media are 54 and 60 mV dec^{-1}, respectively, indicating the involvement of the Volmer–Heyrovsky mechanistic pathway, with Heyrovsky as the RDS. Conversely, in alkaline/neutral media, HESAC–HEA/GO–Fe^{2+} and HESAC–HEA/GO–Fe^{3+} exhibit Tafel values of >120 mV dec^{-1}, signifying that Volmer is the RDS in this case. The remarkable HER activity observed when multiple HESACs and the FeRuPtNiCoPd alloy are coordinated on GO supports may be ascribed to the diverse array of active sites provided by the HESAC and HEA for the HER process, enabling efficient hydrogen adsorption and evolution. Synergistic interactions among various elements in high-entropy systems, including electronic, geometric, and strain effects, further enhance the overall catalytic performance. Additionally, the GO support serves as a stabilizing platform, preventing catalyst aggregation and ensuring access to active sites. Its high electrical conductivity enables effective electron transfer, facilitating rapid kinetics during HER.

The TOF of HESAC–HEA/GO–Fe^{2+} and HESAC–HEA/GO–Fe^{3+} was estimated to reveal their intrinsic electrocatalytic activity. S_a was determined by integrating the total charge from full CV profiles measured in different electrolytes (Fig. S13†). The S_a results of HESAC–HEA/GO–Fe^{2+} showed higher values in all electrolytes 4.05×10^{-6}, 1.94×10^{-6}, and 3.15×10^{-6} mol cm^{-2} in 0.5 M H_2SO_4, 1.0 M KOH, and 0.1 M $KClO_4$, respectively, than HESAC–HEA/GO–Fe^{3+} (1.60×10^{-6}, 1.17×10^{-6}, and 1.40×10^{-6} mol cm^{-2} in 0.5 M H_2SO_4, 1.0 M KOH, and 0.1 M $KClO_4$, respectively). Thus, the high S_a value of HESAC–HEA/GO–Fe^{2+} leads to its improved HER activity. The TOF values estimated at extensive HER potentials for the HESAC–HEA/GO–Fe^{2+} and HESAC–HEA/GO–Fe^{3+} catalysts in different electrolytes are depicted in Fig. S14.† Notably, HESAC–HEA/GO–Fe^{2+} yields a TOF value of 0.037 S^{-1} at −0.1 V *vs.* RHE, while HESAC–HEA/GO–Fe^{3+} yields only 0.021 S^{-1} in 0.5 M H_2SO_4 (Fig. 4d). Concurrently, HESAC–HEA/GO–Fe^{2+} revealed an enhanced mass activity of 29.35 A g^{-1} at −0.1 V *vs.* RHE, which is higher than that of HESAC–HEA/GO–Fe^{3+} (6.57 A g^{-1}) (Fig. 4e and S15†). Thus, the aforementioned TOF, S_a, and mass activity results support the exceptional HER catalytic behavior of HESAC–HEA/GO–Fe^{2+} over HESAC–HEA/GO–Fe^{3+}.

Further, EIS serves as another crucial parameter for assessing HER kinetics, as depicted using the consistent Nyquist plot (Fig. 4f). Moreover, the Nyquist plots obtained were fitted with Z-view software, utilizing the standard Randles equivalent circuit. The equivalent circuit is involving of charge transfer and series resistance (R_{ct} and R_s), along with constant phase element (CPE). The Nyquist curves that were fitted match closely with the results obtained experimentally, as shown in Fig. S16.† The R_{ct} of catalysts was indicated using the appearance of

9080 | *J. Mater. Chem. A*, 2025, **13**, 9073–9087

This journal is © The Royal Society of Chemistry 2025

a high-frequency area in the semicircle of the Nyquist graph. The observed small semicircle in this region signifies reduced resistance and accelerated charge transfer across the electrolyte/electrode interface. HESAC–HEA/GO–Fe^{2+} showed a smaller semicircle and the correspondingly smaller R_{ct} of 2.09 and 5.64 Ω in 0.5 M H$_2$SO$_4$ and 1.0 M KOH, correspondingly, at −0.136 V $vs.$ RHE than HESAC–HEA/GO–Fe^{2+} (2.56 and 9.08 Ω, correspondingly), implying the rapid HER kinetics of HESAC–HEA/GO–Fe^{2+} (Fig. S17†). Furthermore, Bode graphs were utilized to analyze the relaxation or electron lifetimes (τ_e) of the catalysts based on the frequency maximum (f_{max}) at −0.136 V $vs.$ RHE, as illustrated in Fig. 4g. The attained f_{max} for HESAC–HEA/GO–Fe^{2+} was 3.16 and 2.15 Hz in 0.5 M H$_2$SO$_4$ and 1.0 M KOH electrolyte, correspondingly, while for HESAC–HEA/GO–Fe^{3+}, it was 2.61 and 8.25 Hz, respectively. τ_e estimated according to $\tau_e = 1/2\pi f_{max}$ for HESAC–HEA/GO–Fe^{2+} was lower than that obtained for HESAC–HEA/GO–Fe^{3+} in alkaline and acidic media, which is also indicative of the enhanced HER activity of the HESAC–HEA/GO–Fe^{2+} catalyst. Additionally, the exceptional HER activity of HESAC–HEA/GO–Fe^{2+} in 0.5 M H$_2$SO$_4$ was validated with the ECSA value estimated according to ECSA = C_{dl}/C_s, where C_s is the CC capacitance ($\sim$88 mF cm^{-2})[34] and C_{dl} is obtained from non-faradaic CV profiles at diverse scan rates (Fig. S18†). The values of C_{dl} are provided in the scan rate $vs.$ ΔJ/2 plot (Fig. 4h). The estimated ECSA values for HESAC–HEA/GO–Fe^{2+} were 0.98, 0.26, and 0.04 mF cm^{-2}, while HESAC–HEA/GO–Fe^{3+} exhibited ECSA values of 0.33, 0.22, and 0.04 mF cm^{-2} in 0.5 M H$_2$SO$_4$, 1.0 M KOH, and 1 0.1 M KClO$_4$, correspondingly, revealing the high accessible active area of HESAC–HEA/GO–Fe^{2+} toward electrochemical HER activity.

In situ Raman spectroscopy investigation enables the detection of adsorbates on the optimized HESAC–HEA/GO–Fe^{2+} electrocatalyst in 0.5 M H$_2$SO$_4$, providing evidence to support our previous assumption and mechanistic reaction pathway for H$_2$ evolution (Fig. 4i–k). *In situ* electrochemical Raman spectra of HESAC–HEA/GO–Fe^{2+} were measured under a potential portion of 0 to −0.15 V $vs.$ RHE, and the Raman shift was scanned among 300 and 2500 cm^{-1}, as shown in Fig. 4i. The spectra clearly show two peaks at $\sim$1333 and $\sim$1615 cm^{-1} at 0 V $vs.$ RHE, consistent with the D and G bands of GO supports, which also match the *ex situ* Raman results provided in Fig. 1c. Upon increasing the applied potential, additional Raman signals emerge at $\sim$588 and $\sim$1053 cm^{-1} on the surface of HESAC–HEA/GO–Fe^{2+}, which are attributed to Pt–H$_3$O$^+$ interactions.[50] The appearance and strengthening of the Pt–H$_3$O$^+$ interaction peak with increasing applied potential suggest that the H$_3$O$^+$ species detected *via in situ* Raman graphs on the surface of the catalyst are generated through the HER in 0.5 M H$_2$SO$_4$.[51] According to the *in situ* result, the H$_3$O$^+$ formation is directly associated with the H$_2$O dissociation and H$_{ads}$ adsorption process (Volmer step) in the HER, and the proposed HER pathway is depicted in Fig. 4k.

3.3 Electrochemical OER and OWS

The effectiveness of multielement HESAC–HEA/GO–Fe^{2+} and HESAC–HEA/GO–Fe^{3+} as OER catalysts was examined through

a series of catalytic performance tests in different electrolytes: 0.5 M H$_2$SO$_4$, 1.0 M KOH, and 0.1 M KClO$_4$ solutions. Fig. 5a illustrates the OER LSV curves of HESAC–HEA/GO–Fe^{2+} and HESAC–HEA/GO–Fe^{3+} in different electrolytes. The HESAC–HEA/GO–Fe^{2+} catalyst showed a smaller η of 398 and 544 mV at 10 and 50 mA cm^{-2} in 1.0 M KOH than those of HESAC–HEA/GO–Fe^{3+} and comparable with commercial RuO$_2$ catalyst (Fig. 5b and S19†). Fig. 5b reveals that the enhancement in HESAC–HEA/GO–Fe^{2+} improves its OER in 1.0 M KOH compared with the other two solutions. This improvement may be attributed to the alkaline environment provided by the KOH solution, which offers a higher concentration of hydroxide ions, facilitating the establishment of O-intermediates and promoting the OER process. Additionally, the alkaline conditions in the KOH solution create a favorable environment for the evolution of oxygen species from the HESAC–HEA/GO–Fe^{2+} catalyst surface, leading to enhanced OER kinetics. Moreover, the stability of active intermediates involved in the OER process may be better maintained in an alkaline environment compared with acidic or neutral conditions.

The investigation of OER kinetics for various electrolytes was conducted by generating Tafel plots from the LSV curves of the HESAC–HEA/GO–Fe^{2+} and HESAC–HEA/GO–Fe^{3+}catalysts. As depicted in Fig. 5c and S20,† HESAC–HEA/GO–Fe^{2+} exhibited a remarkably lower Tafel slope of 87, 330, 597 mV dec^{-1} in 1.0 M KOH, 0.5 M H$_2$SO$_4$, and 0.1 M KClO$_4$, correspondingly, than HESAC–HEA/GO–Fe^{3+} (90, 348, 602 mV dec^{-1}, respectively). The superior OER activity of HESAC–HEA/GO–Fe^{2+} is attributed to the presence of multiple single-atomic sites, while the high-entropy alloy (HEA) structure provides a diverse array of active sites for the OER process. These active sites facilitate the adsorption/activation of O-species, thereby enhancing overall OER kinetics. Additionally, synergistic interactions among the various elements in the high-entropy system further improve the catalytic reactivity. In the FeRuPtNiCoPd (HESAC–HEA) system, these synergistic effects play a crucial role in boosting OER performance. The compositional complexity of FeRuPtNiCoPd HESAC–HEA modulates the electronic structure, optimizing the binding energies of key OER intermediates (*OH, *O, and *OOH) and thereby accelerating reaction kinetics. Lattice strain effects, induced by atomic size mismatches, create a distorted local environment that enhances intermediate adsorption and desorption behavior, effectively lowering the overpotential. Specific elements contribute distinct functionalities: Ru and Co enhance the intrinsic OER activity, Fe and Ni synergistically improve catalytic efficiency–particularly in alkaline media–while Pt and Pd primarily stabilize and fine-tune the electronic and structural properties of the catalyst, further optimizing its OER performance.[52] The GO support serves to anchor and stabilize catalyst species, ensuring their dispersion and the obtainability of active sites in the catalyst. Moreover, the high electrical conductivity of GO facilitates efficient electron transfer during OER, thereby enabling rapid reaction kinetics.

Catalytic efficiency, mainly characterized by intrinsic catalytic action and the exposure of active sites, was assessed quantitatively using TOF and R_{ct} as pivotal metrics in electrocatalysis.[53] The evaluated TOF at various OER potentials for the HESAC–HEA/GO–Fe^{2+} and HESAC–HEA/GO–Fe^{3+} catalysts in different
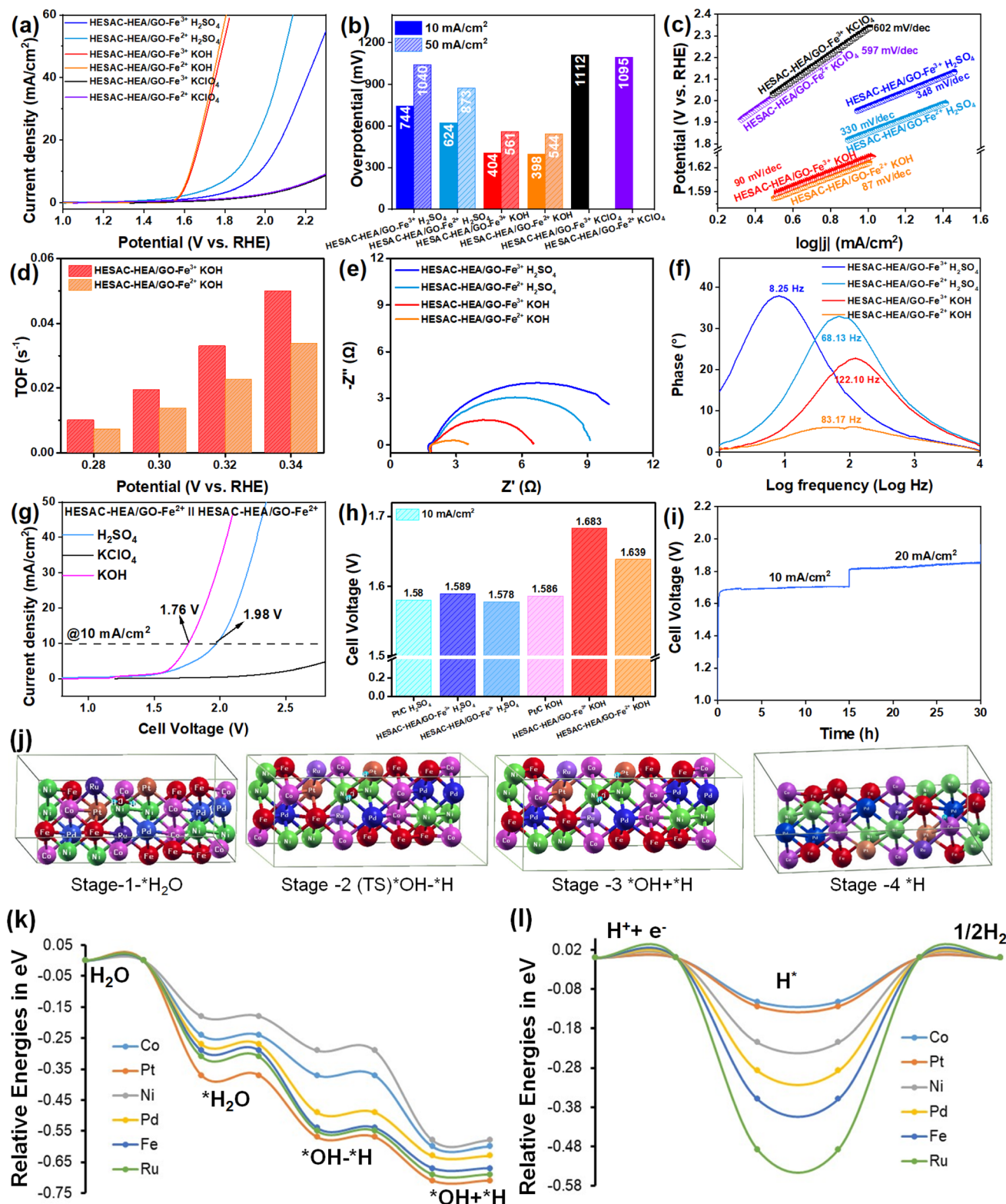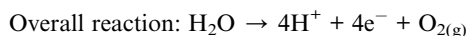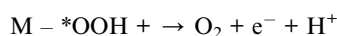
Fig. 5 (a) OER graphs of HESAC−HEA/GO−Fe^{2+} and HESAC−HEA/GO−Fe^{3+} in 0.5 M H$_2$SO$_4$, 1.0 M KOH, and 1 0.1 M KClO$_4$ solutions at 5 mV s^{-1} (b) η at 10 and 50 mA cm^{-2}, (c) Tafel slope, (d) TOF, (e and f) Nyquist and Bode plots, and (g) polarization curves of the HESAC−HEA/GO−Fe^{2+}∥HESAC−HEA/GO−Fe^{2+} electrolyzer OWS in 0.5 M H$_2$SO$_4$, 1.0 M KOH, and 0.1 M KClO$_4$. (h) Cell voltage required to attain 10 mA cm^{-2}, (i) step-stability test of HESAC−HEA/GO−Fe^{2+}∥HESAC−HEA/GO−Fe^{2+} in 1.0 M KOH at different current densities, (j) the atomic arrangements at catalytic sites of the FeRuPtNiCoPd HEA in HESAC−HEA/GO in four different stages, (k) reaction energy profile for H$_2$O dissociation, and (l) H-adsorption on several catalytic sites of CoFeNiPtPdRu (k1) HEA surface.

9082 | J. Mater. Chem. A, 2025, **13**, 9073–9087

This journal is © The Royal Society of Chemistry 2025

electrolytes are depicted in Fig. S21.† Notably, HESAC–HEA/GO–Fe^{2+} yielded a TOF value of 0.049 S^{-1} at 0.34 V vs. RHE, while HESAC–HEA/GO–Fe^{3+} yielded only 0.033 S^{-1} in 1.0 M KOH (Fig. 5d). The R_{ct} of HESAC–HEA/GO–Fe^{2+} determined from the Nyquist impedance graph shown in Fig. 5e was ∼1.74 and ∼7.31 Ω, while HESAC–HEA/GO–Fe^{3+} showed 4.65 and 8.32 Ω in 1.0 M KOH and 0.5 M H_2SO_4 electrolytes, correspondingly. Thus, the fitted Nyquist impedance plot using the Randles equivalent circuit is shown in Fig. S22,† and for better clarity, the estimated R_{ct} values are also plotted in Fig. S23.† Concurrently, HESAC–HEA/GO–Fe^{2+} revealed an enhanced mass activity at applied wide range of OER potential, which is higher than that of HESAC–HEA/GO–Fe^{3+} (Fig. S24†). The pattern of high TOF and low R_{ct} values for HESAC–HEA/GO–Fe^{2+} in 1.0 M KOH suggests that the synergistic influence of multiple elements can expedite electron transport and OER kinetics. Furthermore, τ_e estimated using f_{max} from Bode curves proves that the optimized HESAC–HEA/GO–Fe^{2+} catalyst in 1.0 M KOH has τ_e values of 0.0019 and 0.0023 s in 1.0 M KOH and 0.5 M H_2SO_4, correspondingly, while that of HESAC–HEA/GO–Fe^{3+} was 0.0013 and 0.019 s, respectively, supporting the enhanced OER kinetics of the HESAC–HEA/GO–Fe^{2+} electrocatalyst (Fig. 5f).
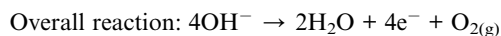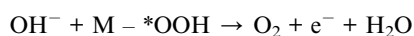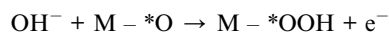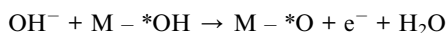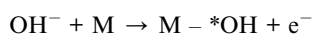
In alkaline, acidic, and neutral media, the OER mechanism may differ owing to differences in pH, ion concentrations, and potential energy landscapes. Similar to HER, the reaction pathway involved in the alkaline/neutral conditions remains nearly the same, with hydroxide ions potentially playing an important role, while in acidic conditions, proton-coupled electron transfer (PCET) mechanisms may dominate the reaction.[54]

In acidic electrolytes,

$$H_2O + M \rightarrow M - *OH + e^- + H^+$$

$$M - OH_{ads} \rightarrow M - *O + e^- + H^+$$

$$M - *O + H_2O \rightarrow M - *OOH + e^- + H^+$$

$$M - *OOH + \rightarrow O_2 + e^- + H^+$$

$$\text{Overall reaction: } H_2O \rightarrow 4H^+ + 4e^- + O_{2(g)}$$
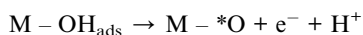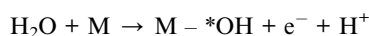
In acidic solutions, the mechanism of the OER typically involves four concerted PCET processes with oxygenated intermediates on catalytic active sites (M = HESAC–HEA/GO–Fe^{2+} and HESAC–HEA/GO–Fe^{3+}), such as *OH, *O, and *OOH. Initially, H_2O molecules undergo oxidation to produce oxygen molecules, H^+, and e^-. This process is facilitated by the presence of a catalyst, which provides active sites for H_2O oxidation.

In alkaline/neutral electrolytes,

$$OH^- + M \rightarrow M - *OH + e^-$$

$$OH^- + M - *OH \rightarrow M - *O + e^- + H_2O$$

$$OH^- + M - *O \rightarrow M - *OOH + e^-$$

$$OH^- + M - *OOH \rightarrow O_2 + e^- + H_2O$$

$$\text{Overall reaction: } 4OH^- \rightarrow 2H_2O + 4e^- + O_{2(g)}$$

In alkaline/neutral solutions, OH^- adsorbs on the electrocatalyst surface sites via one e^--oxidation process, generating M – *OH intermediates, which then react with OH^- to produce M – *O intermediates. Subsequently, *O species couples with OH^- to form *OOH intermediate products, leading to the release of O_2 gas via the deprotonation process. Typically, electrocatalysts based on transition metals tend to generate uniform (hydro) oxide intermediates during OER in basic solutions.[34]

HESAC–HEA/GO–Fe^{2+}, known for its remarkable catalytic activity for OER and HER, was employed as the anode and cathode (HESAC–HEA/GO–Fe^{2+}‖HESAC–HEA/GO–Fe^{2+}) for fabricating the electrolyzer for OWS across different electrolytes, including 0.5 M H_2SO_4, 1.0 M KOH, and 0.1 M $KClO_4$, and its polarization curves are shown in Fig. 5g. The fabricated OWS electrolyzer required a cell voltage of 1.76 and 1.98 V to deliver 10 mA cm^{-2} in 1.0 M KOH and 0.5 M H_2SO_4, correspondingly, while the cell's OWS performance in 0.1 M $KClO_4$ was negligible (Fig. 5g). Also, the cell voltage at different current density for the fabricated HESAC–HEA/GO–Fe^{2+}‖HESAC–HEA/GO–Fe^{2+} electrolyzer in 1.0 M KOH and 0.5 M H_2SO_4 electrolytes is plotted in Fig. S25.† For comparison, IrO_2‖Pt/C, IrO_2‖HESAC–HEA/GO–Fe^{2+}, and IrO_2‖HESAC–HEA/GO–Fe^{3+} were fabricated, and the resulting polarization curves and cell voltage obtained in 0.5 M H_2SO_4 and 1.0 M KOH electrolytes are displayed in Fig. 5h and S26†. In Fig. S27,† images of the fabricated electrolyzer are displayed. The membrane-less single-compartment electrolyzer presents several advantages over H-cell configurations with membranes. First, its simplified design reduces manufacturing complexity and cost. Second, it boasts enhanced durability owing to the absence of membrane-related degradation or fouling. Additionally, the elimination of membrane-induced resistance allows for improved ion transport, resulting in high current densities and increased efficiency in the membrane-less electrolyzer device. Furthermore, maintenance is simplified in this case as there is no need to replace or clean membranes periodically. They also mitigate the risk of gas crossover, enhancing safety and efficiency. HESAC–HEA/GO–Fe^{2+}‖HESAC–HEA/GO–Fe^{2+} demonstrated remarkable long-term step stability, serving as a highly effective bifunctional substance for more than 30 h at different current densities of 10 mA cm^{-2} and 20 mA cm^{-2}. As depicted in Fig. 5i, the electrode maintained a nearly constant cell voltage during the delivery of these specified current densities, highlighting its outstanding long-term electrochemical durability. Remarkably, the HER and OER performance of the fabricated HESAC–HEA/GO–Fe^{2+} sample was greater if not comparable than previous reported HEA-based electrocatalysts, as detailed in Table S2 and S3.† The stability of electrocatalysts is a critical factor in their assessment, particularly for HEAs, where maintaining configurational entropy (ΔS) plays a crucial role in structural and electrochemical stability. Based on ΔS values, materials are classified as low-entropy ($\Delta S \leq 0.7R$), medium-entropy ($0.7R \leq \Delta S \leq 1.5R$), and high-entropy alloys ($\Delta S \geq 1.5R$).[52,55] The configurational entropy is calculated using the formula

This journal is © The Royal Society of Chemistry 2025

J. Mater. Chem. A, 2025, **13**, 9073–9087 | **9083**

Journal of Materials Chemistry A

Paper

$$\Delta S = -R \sum_{i=1}^{n} x_i \ln(x_i),$$

where R refers the gas constant and x_i represents the molar fraction of the ith element. The calculated entropy values indicate that HESAC–HEA/GO–Fe^{2+} exhibits the highest ΔS (1.65R), demonstrating superior high-entropy stabilization compared to HESAC–HEA/GO–Fe^{3+} ($\Delta S = 1.62R$).

The HESAC–HEA/GO–Fe^{2+} electrode material deposited on CC was subjected to post-characterization using FESEM, EDS, and XPS analyses following the OWS stability test. As shown in Fig. S28,† the surface morphology and elemental composition of the HESAC–HEA/GO–Fe^{2+}/CC employed at the anode of HESAC–HEA/GO–Fe^{2+}||HESAC–HEA/GO–Fe^{2+} electrolyzer system were examined. The FESEM image (Fig. S28a†) confirms that the uniformly distributed HESAC–HEA on the GO support remained intact even after 30 h of continuous electrolysis with some observable aggregates, likely resulting from interactions between the electrode surface and the electrolyte solution. The EDS elemental mapping (Fig. S28b†) further demonstrates the homogeneous distribution of the six metal elements–Co, Fe, Ni, Pt, Pd, and Ru–along with C and O from the GO support. Notably, the oxygen content increased after the OWS test compared to the pristine HESAC–HEA/GO–Fe^{2+} sample, suggesting that the HESAC–HEA/GO–Fe^{2+}/CC electrode underwent surface oxidation during the OER process, thereby further supporting the proposed OER mechanism in alkaline media. To probe the surface states and chemical composition of the HESAC–HEA/GO–Fe^{2+} catalyst after prolonged OWS testing, post-XPS analysis was conducted on the HESAC–HEA/GO–Fe^{2+}/CC electrode used as the anode. The XPS survey spectrum (Fig. S29a–i†) confirmed the presence of Co, Fe, Ni, Pt, Pd, Ru, C, and O, consistent with the EDS results. Following the OWS stability test, the XPS survey spectrum (Fig. S29a†) also revealed a prominent F 1s signal, originating from Nafion, which was used as a binder in the fabrication of the HESAC–HEA/GO–Fe^{2+} electrode on the CC substrate. Additionally, the characteristic metal peaks corresponding to Co, Fe, Ni, Pt, Pd, and Ru exhibited reduced intensity compared to the pristine HESAC–HEA/GO–Fe^{2+} sample (Fig. S29d–i†).[56] No distinct Fe 2p signal was detected, likely due to the overlapping of the F 1s spectrum from the Nafion binder (Fig. S29e†). The O 1s spectrum was deconvoluted into three peaks corresponding to lattice metal (Me)–oxygen (Me–O), oxygen associated with hydroxyl groups and oxyhydroxide species located at 531.1, 532.5, and 534.0 eV, respectively (Fig. S29c†). Notably, the intensity of peaks related with lattice oxygen and oxyhydroxide species increased significantly compared to the pristine HESAC–HEA/GO–Fe^{2+} sample. This observation confirms the formation of a metal–OOH layer on the HESAC–HEA/GO–Fe^{2+} surface during the electrochemical OWS process in 1.0 M KOH solution.[57,58]

3.4 Computational studies

We conducted DFT calculations to finalize the multiple active sites cooperation in the alkaline HER. Various configurations of HESAC-HEA/GO periodic systems were generated, and the lowest energy configuration was used for catalytic active site studies. The configuration with maximum asymmetry is more stable by 1.2 eV than other structures, as shown in Fig. S30.† Charge analysis indicates that, on average, Co (−0.7 e), Fe (−0.3 e), and Ni (−0.2 e) have more negative charges than Pt (0.8 e), Pd (0.7 e), and Ru (0.3 e), supporting the completely polarized structures. Fig. 5j illustrates the atomic arrangements at the catalytic sites of the FeRuPtNiCoPd HEA in four stages. The different metals stabilize the HEA with larger stabilization energy. The water molecule (H$_2$O*) adsorbed on the HEA surface (stage 1) undergoes H–OH bond destabilization (stage 2), then dissociates to produce OH* and H* species coadsorption (stage 3). The H* intermediate detaches from the surface after combining with additional H* to produce H$_2$ in the final stage. The H$_2$O dissociation into OH* and H* and the H* adsorption is RDS that influences H$_2$O dissociation rates. The FeRuPtNiCoPd HEA structures are depicted in Fig. S30.† Fig. 5k displays the energy profile for H$_2$O dissociation on Fe, Ni, Co, Pt, Pd, and Ru sites for the k1 configuration, while Fig. S31† shows the energy profile for the k1a configuration. Additionally, Fig. S32 and S33† show the structures and various atomic arrangements of HEA during H$_2$O dissociation. Remarkably, the energy barriers for H–OH breaking (stage 1 → stage 2) on Ni and Co sites of HEA are the lowest, at 0.29 and 0.37 eV, respectively, compared to Pd (0.49 eV), Fe (0.54 eV), Ru (0.72 eV), and Pt (0.82 eV). These results suggest that H$_2$O adsorption and dissociation are more favorable at Co and Ni sites, which accelerates H$_2$O dissociation and the production of H* species. Similarly, in the k1a configuration, Ni and Co are preferred for adsorption and dissociation.

In addition, we calculated the relative energies of adsorbed atomic hydrogen (ΔE_{H}) at four catalytic sites of HEA to understand the impact of diverse sites on H* adsorption, as shown in Fig. 5l. The atomic arrangements of the FeRuPtNiCoPd HEA at the H* adsorption stage on all metal sites are shown in Fig. S32 and S33.† The DFT outcomes specified that Co sites achieve the most favorable ΔE_{H} of −0.112 eV, compared to Pt (−0.12 eV), Ni (−0.22 eV), Pd (−0.29 eV), Fe (−0.36 eV), and Ru (−0.49 eV). This suggests that H* is especially stabilized at Co and Pt sites. During the entire OWS process, the Co, Ni, and Pt sites work together to facilitate H$_2$O dissociation and H* adsorption with the lowest energies, preventing the blocking of active sites and accelerating the overall H$_2$O dissociation process.

4. Conclusion

The high-entropy multimetallic FeRuPtNiCoPd single-atomic sites and HEA co-coordinated on GO supports were synthesized *via* a single-pot PLIL process. HESAC–HEA/GO exhibits excellent multifunctional HER, OER, and OWS catalytic activity across a wide pH range. Co, Ni, and Pt sites synergistically accelerate H$_2$O dissociation and H* adsorption, enhancing overall water splitting efficiency in the HESAC–HEA/GO. In particular, the synergistic inherent interactions in high-entropy systems, coupled with the rapid photoreduction of Fe^{2+} facilitated by the PLIL process, lead to the greater generation of nuclei and active sites in HESAC–HEA/GO–Fe^{2+} compared to

9084 | *J. Mater. Chem. A*, 2025, **13**, 9073–9087

This journal is © The Royal Society of Chemistry 2025

Fe^{3+} (HESAC–HEA/GO–Fe^{2+}). This phenomenon enhances the catalytic activity of HESAC–HEA/GO–Fe^{2+} for the HER, achieving η values of 49 and 150 mV at 10 mA cm^{-2} in 0.5 M H_2SO_4 and 1.0 M KOH, correspondingly, alongside record-high OER with η values of 624 and 398 mV at 10 mA cm^{-2} in 0.5 M H_2SO_4 and 1.0 M KOH, correspondingly. When utilized for OWS, HESAC–HEA/GO–Fe^{2+}∥HESAC–HEA/GO–Fe^{2+} attains 10 mA cm^{-2} at 1.76 and 1.97 V in 1.0 M KOH and 0.5 M H_2SO_4, correspondingly. The selectivity of the electrode with HESAC–HEA/GO–Fe^{2+}∥Pt/C substantially decreases the cell voltage to 1.58 V in 1.0 M KOH. *In situ* Raman and DFT investigations unveil that the surface composition of multielement HESACC–HEA/GO and their active sites not only facilitate highly efficient electron transfer but also tune the electronic structures of the catalyst, enhancing the oxidation and reduction performance crucial for OWS. HESAC–HEA/GO–Fe^{2+}∥HESAC–HEA/GO–Fe^{2+} demonstrates remarkable long-term stability, serving as an effective multi-functional electrocatalyst for OWS.

Data availability

The data supporting this article have been included as part of the ESI.†

Conflicts of interest

No conflict to declare.

Acknowledgements

References

1 K. Sun, Y. Huang, F. Sun, Q. Wang, Y. Zhou, J. Wang, Q. Zhang, X. Zheng, F. Fan, Y. Luo, J. Jiang and H.-L. Jiang, Dynamic structural twist in metal–organic frameworks enhances solar overall water splitting, *Nat. Chem.*, 2024, **16**, 1638–1646.

2 Y. Oh, J. Theerthagiri, M. L. Aruna Kumari, A. Min, C. J. Moon and M. Y. Choi, Electrokinetic-mechanism of water and furfural oxidation on pulsed laser-interlaced Cu_2O and CoO on nickel foam, *J. Energy Chem.*, 2024, **91**, 145–154.

3 Z. Wu, Q. Li, G. Xu, W. Jin, W. Xiao, Z. Li, T. Ma, S. Feng and L. Wang, Microwave Phosphine-Plasma-Assisted Ultrafast Synthesis of Halogen-Doped Ru/RuP_2 with Surface Intermediate Adsorption Modulation for Efficient Alkaline Hydrogen Evolution Reaction, *Adv. Mater.*, 2024, **36**, 2311018.

4 M. S. A. Sher Shah, G. Y. Jang, K. Zhang and J. H. Park, Transition metal carbide-based nanostructures for electrochemical hydrogen and oxygen evolution reactions, *EcoEnergy*, 2023, **1**, 344–374.

5 Y.-N. Zhou, W.-L. Yu, H.-J. Liu, R.-Y. Fan, G.-Q. Han, B. Dong and Y.-M. Chai, Self-integration exactly constructing oxygen-modified MoNi alloys for efficient hydrogen evolution, *EcoEnergy*, 2023, **1**, 425–436.

6 R. Yin, Z. Wang, J. Zhang, W. Liu, J. He, G. Hu and X. Liu, Tunable NiSe-Ni_3Se_2 Heterojunction for Energy-Efficient Hydrogen Production by Coupling Urea Degradation, *Small Methods*, 2025, 2401976.

7 A. Kumar, V. Q. Bui, J. Lee, L. Wang, A. R. Jadhav, X. Liu, X. Shao, Y. Liu, J. Yu, Y. Hwang, H. T. D. Bui, S. Ajmal, M. G. Kim, S.-G. Kim, G.-S. Park, Y. Kawazoe and H. Lee, Moving beyond bimetallic-alloy to single-atom dimer atomic-interface for all-pH hydrogen evolution, *Nat. Commun.*, 2021, **12**, 6766.

8 W. Jin, H. Wu, W. Cai, B. Jia, M. Batmunkh, Z. Wu and T. Ma, Evolution of interfacial coupling interaction of Ni-Ru species for pH-universal water splitting, *Chem. Eng. J.*, 2021, **426**, 130762.

9 L. Chen, J.-T. Ren and Z.-Y. Yuan, Interface engineering for boosting electrocatalytic performance of CoP-Co_2P polymorphs for all-pH hydrogen evolution reaction and alkaline overall water splitting, *Sci. China Mater.*, 2022, **65**, 2433–2444.

10 H. Lee, J. Theerthagiri, M. L. Aruna Kumari, A. Min, C. J. Moon, V. Anbazhagan, R. L. Brutchey and M. Y. Choi, Leveraging phosphate group in Pd/PdO decorated nickel phosphate microflowers via pulsed laser for robust hydrogen production in hydrazine-assisted electrolyzer, *Int. J. Hydrogen Energy*, 2024, **57**, 176–186.

11 J. Theerthagiri, K. Karuppasamy, C. Justin Raj, G. Maia, M. L. Aruna Kumari, L. John Kennedy, M. K. R. Souza, E. S. F. Cardoso, S. Kheawhom, H.-S. Kim and M. Y. Choi, Structural engineering of metal oxyhydroxide for electrochemical energy conversion and storage, *Coord. Chem. Rev.*, 2024, **513**, 215880.

12 P. Yang, F. Liu, X. Zang, L. Xin, W. Xiao, G. Xu, H. Li, Z. Li, T. Ma, J. Wang, Z. Wu and L. Wang, Microwave Quasi-Solid State to Construct Strong Metal-Support Interactions with Interfacial Electron-Enriched Ru for Anion Exchange Membrane Electrolysis, *Adv. Energy Mater.*, 2024, **14**, 2303384.

13 Y. Wang, J. Li, P. Yang, H. Li, G. Xu, Y. Du, C. Li, W. Jin, T. Ma, Z. Wu and L. Wang, Interfacial Ru nanoclusters in tandem with single atoms on oxygen-vacancy regulated CeO_2 for anion exchange membrane seawater-splitting, *J. Energy Chem.*, 2025, **102**, 618–627.

This journal is © The Royal Society of Chemistry 2025

J. Mater. Chem. A, 2025, **13**, 9073–9087 | **9085**

14 J. Ding, Z. Peng, Z. Wang, C. Zeng, Y. Feng, M. Yang, G. Hu, J. Luo and X. Liu, Phosphorus–tungsten dual-doping boosts acidic overall seawater splitting performance over RuO_x nanocrystals, *J. Mater. Chem. A*, 2024, **12**, 28023–28031.

15 J. Hao, Z. Zhuang, K. Cao, G. Gao, C. Wang, F. Lai, S. Lu, P. Ma, W. Dong, T. Liu, M. Du and H. Zhu, Unraveling the electronegativity-dominated intermediate adsorption on high-entropy alloy electrocatalysts, *Nat. Commun.*, 2022, **13**, 2662.

16 R. Zhou, X. Han, Q. Chen, L. Peng, X. Qiu, P. Wang, C. Guo, J. Wang, Z. Wang and J. Hao, Surface decoration on self-supporting high entropy alloy electrodes for enhanced electrochemical water splitting, *J. Mater. Chem. A*, 2024, **12**, 5719–5730.

17 Q. Zhang, K. Lian, Q. Liu, G. Qi, S. Zhang, J. Luo and X. Liu, High entropy alloy nanoparticles as efficient catalysts for alkaline overall seawater splitting and Zn-air batteries, *J. Colloid Interface Sci.*, 2023, **646**, 844–854.

18 H. Zhu, S. Sun, J. Hao, Z. Zhuang, S. Zhang, T. Wang, Q. Kang, S. Lu, X. Wang, F. Lai, T. Liu, G. Gao, M. Du and D. Wang, A high-entropy atomic environment converts inactive to active sites for electrocatalysis, *Energy Environ. Sci.*, 2023, **16**, 619–628.

19 M. D. Symes and L. Cronin, Decoupling hydrogen and oxygen evolution during electrolytic water splitting using an electron-coupled-proton buffer, *Nat. Chem.*, 2013, **5**, 403–409.

20 J. Pei, H. Shang, J. Mao, Z. Chen, R. Sui, X. Zhang, D. Zhou, Y. Wang, F. Zhang, W. Zhu, T. Wang, W. Chen and Z. Zhuang, A replacement strategy for regulating local environment of single-atom $Co-S_xN_{4-x}$ catalysts to facilitate CO_2 electroreduction, *Nat. Commun.*, 2024, **15**, 416.

21 S. Guan, Z. Yuan, Z. Zhuang, H. Zhang, H. Wen, Y. Fan, B. Li, D. Wang and B. Liu, Why do Single-Atom Alloys Catalysts Outperform both Single-Atom Catalysts and Nanocatalysts on MXene?, *Angew. Chem., Int. Ed.*, 2024, **63**, e202316550.

22 P. Rao, Y. Deng, W. Fan, J. Luo, P. Deng, J. Li, Y. Shen and X. Tian, Movable type printing method to synthesize high-entropy single-atom catalysts, *Nat. Commun.*, 2022, **13**, 5071.

23 X. Wang, L. Xu, C. Li, C. Zhang, H. Yao, R. Xu, P. Cui, X. Zheng, M. Gu, J. Lee, H. Jiang and M. Huang, Developing a class of dual atom materials for multifunctional catalytic reactions, *Nat. Commun.*, 2023, **14**, 7210.

24 Q. Yang, W. Wang, Y. Zhou, J. Hao, G. Fang, C. Liu, P. Cui and Y. Wang, Facile Pyrolysis Treatment for the Synthesis of Single-Atom Mn Catalysts Derived from a Hyperaccumulator, *ACS ES&T Eng.*, 2023, **3**, 616–626.

25 P. Yin and B. You, Atom migration-trapping toward single-atom catalysts for energy electrocatalysis, *Mater. Today Energy*, 2021, **19**, 100586.

26 J. Fonseca and J. Lu, Single-Atom Catalysts Designed and Prepared by the Atomic Layer Deposition Technique, *ACS Catal.*, 2021, **11**, 7018–7059.

27 W. Liu, H. Zhang, C. Li, X. Wang, J. Liu and X. Zhang, Non-noble metal single-atom catalysts prepared by wet chemical method and their applications in electrochemical water splitting, *J. Energy Chem.*, 2020, **47**, 333–345.

28 Y. Lee, J. Theerthagiri, A. Min, C. J. Moon and M. Y. Choi, Dual-laser pulse-patterned α-Co(OH)2/rGO heterointerface for accelerated water oxidation and surface phase-transition via in-situ Raman spectroscopy, *EcoMat*, 2023, **5**, e12417.

29 Y. Yu, S. J. Lee, J. Theerthagiri, Y. Lee and M. Y. Choi, Architecting the AuPt alloys for hydrazine oxidation as an anolyte in fuel cell: Comparative analysis of hydrazine splitting and water splitting for energy-saving H_2 generation, *Appl. Catal., B*, 2022, **316**, 121603.

30 Y. Jeong, S. S. Naik, J. Theerthagiri, C. J. Moon, A. Min, M. L. Aruna Kumari and M. Y. Choi, Manifolding surface sites of compositional CoPd alloys via pulsed laser for hydrazine oxidation-assisted energy-saving electrolyzer: Activity origin and mechanism discovery, *Chem. Eng. J.*, 2023, **470**, 144034.

31 J. Theerthagiri, K. Karuppasamy, A. Min, D. Govindarajan, M. L. A. Kumari, G. Muthusamy, S. Kheawhom, H.-S. Kim and M. Y. Choi, Unraveling the fundamentals of pulsed laser-assisted synthesis of nanomaterials in liquids: Applications in energy and the environment, *Appl. Phys. Rev.*, 2022, **9**, 041314.

32 J. Theerthagiri, K. Karuppasamy, S. J. Lee, R. Shwetharani, H.-S. Kim, S. K. K. Pasha, M. Ashokkumar and M. Y. Choi, Fundamentals and comprehensive insights on pulsed laser synthesis of advanced materials for diverse photo- and electrocatalytic applications, *Light: Sci. Appl.*, 2022, **11**, 250.

33 M.-C. Hsiao, S.-H. Liao, M.-Y. Yen, P.-I. Liu, N.-W. Pu, C.-A. Wang and C.-C. M. Ma, Preparation of Covalently Functionalized Graphene Using Residual Oxygen-Containing Functional Groups, *ACS Appl. Mater. Interfaces*, 2010, **2**, 3092–3099.

34 Y. Oh, J. Theerthagiri, A. Min, C. J. Moon, Y. Yu and M. Y. Choi, Pulsed laser interference patterning of transition-metal carbides for stable alkaline water electrolysis kinetics, *Carbon Energy*, 2024, **6**, e448.

35 R. S. Mishra, R. S. Haridas and P. Agrawal, High entropy alloys – Tunability of deformation mechanisms through integration of compositional and microstructural domains, *Mater. Sci. Eng., A*, 2021, **812**, 141085.

36 Q. Lai, S. Zhu, X. Luo, M. Zou and S. Huang, Ultraviolet-visible spectroscopy of graphene oxides, *AIP Adv.*, 2012, **2**, 032146.

37 M. Hashemi, M. H. Farzad, N. Asger Mortensen and S. Xiao, Enhanced absorption of graphene in the visible region by use of plasmonic nanostructures, *J. Opt.*, 2013, **15**, 055003.

38 A. Hernández-Ramírez, N. M. Sánchez-Padilla, R. Benavides, L. Da Silva and D. Morales-Acosta, Reduced Graphene Oxide-Magnetite for the Development of Highly Active, Selective and Methanol-Tolerant Pt Catalyst, *J. Inorg. Organomet. Polym. Mater.*, 2025, **35**, 87–97.

39 M. Hayyan, A. Abo-Hamad, M. A. AlSaadi and M. A. Hashim, Functionalization of graphene using deep eutectic solvents, *Nanoscale Res. Lett.*, 2015, **10**, 324.

40 S. Muralikrishna, K. Sureshkumar, T. S. Varley, D. H. Nagaraju and T. Ramakrishnappa, In situ reduction and functionalization of graphene oxide with l-cysteine for simultaneous electrochemical determination of cadmium(ii), lead(ii), copper(ii), and mercury(ii) ions, *Anal. Methods*, 2014, **6**, 8698–8705.

41 K. Alam, Y. Sim, J.-H. Yu, J. Gnanaprakasam, H. Choi, Y. Chae, U. Sim and H. Cho, In-situ Deposition of Graphene Oxide Catalyst for Efficient Photoelectrochemical Hydrogen Evolution Reaction Using Atmospheric Plasma, *Materials*, 2020, **13**, 12.

42 T. X. Nguyen, Y.-C. Liao, C.-C. Lin, Y.-H. Su and J.-M. Ting, Advanced High Entropy Perovskite Oxide Electrocatalyst for Oxygen Evolution Reaction, *Adv. Funct. Mater.*, 2021, **31**, 2101632.

43 T. Begildayeva, J. Theerthagiri, S. J. Lee, Y. Yu and M. Y. Choi, Unraveling the Synergy of Anion Modulation on Co Electrocatalysts by Pulsed Laser for Water Splitting: Intermediate Capturing by In Situ/Operando Raman Studies, *Small*, 2022, **18**, 2204309.

44 S. Jiang, K. Tian, X. Li, C. Duan, D. Wang, Z. Wang, H. Sun, R. Zheng and Y. Liu, Amorphous High-entropy Non-precious metal oxides with surface reconstruction toward highly efficient and durable catalyst for oxygen evolution reaction, *J. Colloid Interface Sci.*, 2022, **606**, 635–644.

45 T. X. Nguyen, Y.-H. Su, C.-C. Lin, J. Ruan and J.-M. Ting, A New High Entropy Glycerate for High Performance Oxygen Evolution Reaction, *Adv. Sci.*, 2021, **8**, 2002446.

46 M. Tamtaji, M. G. Kim, J. Wang, P. R. Galligan, H. Zhu, F.-F. Hung, Z. Xu, Y. Zhu, Z. Luo, W. A. Goddard and G. Chen, A High-Entropy Single-Atom Catalyst Toward Oxygen Reduction Reaction in Acidic and Alkaline Conditions, *Adv. Sci.*, 2024, 2309883.

47 B.-W. Zhang, T. Zheng, Y.-X. Wang, Y. Du, S.-Q. Chu, Z. Xia, R. Amal, S.-X. Dou and L. Dai, Highly efficient and selective electrocatalytic hydrogen peroxide production on Co-O-C active centers on graphene oxide, *Commun. Chem.*, 2022, **5**, 43.

48 S. Jayabal, G. Saranya, J. Wu, Y. Liu, D. Geng and X. Meng, Understanding the high-electrocatalytic performance of two-dimensional MoS_2 nanosheets and their composite materials, *J. Mater. Chem. A*, 2017, **5**, 24540–24563.

49 M. Ďurovič, J. Hnát and K. Bouzek, Electrocatalysts for the hydrogen evolution reaction in alkaline and neutral media. A comparative review, *J. Power Sources*, 2021, **493**, 229708.

50 I. S. Lee and S. Sekhar Nanda, Proton Transfer Reaction in Water: Hydronium Ion Formation, *Adv. J. Chem., Sect. A*, 2020, **3**, 255–258.

51 X. Wang, C. Xu, M. Jaroniec, Y. Zheng and S.-Z. Qiao, Anomalous hydrogen evolution behavior in high-pH environment induced by locally generated hydronium ions, *Nat. Commun.*, 2019, **10**, 4876.

52 C. E. Park, J. Theerthagiri, V. Maheskumar, A. Kumar, G. H. Jeong and M. Y. Choi, Cocktail Effect of 4d/5d Band Twisted High-Entropy Alloys on Carbon Nanotube for Hydrazine Splitting, *Small*, 2025, 2410304.

53 T. Zhang, J. Li, B. Zhang, G. Wang, K. Jiang, Z. Zheng and J. Shen, High-entropy alloy CuCrFeNiCoP film of Cu-based as high-efficiency electrocatalyst for water splitting, *J. Alloys Compd.*, 2023, **969**, 172439.

54 C. Wang, Q. Zhang, B. Yan, B. You, J. Zheng, L. Feng, C. Zhang, S. Jiang, W. Chen and S. He, Facet Engineering of Advanced Electrocatalysts Toward Hydrogen/Oxygen Evolution Reactions, *Nano-Micro Lett.*, 2023, **15**, 52.

55 Y. Sun and S. Dai, High-entropy materials for catalysis: A new frontier, *Sci. Adv.*, 2021, **7**, eabg1600.

56 T. Begildayeva, J. Theerthagiri, W. Limphirat, A. Min, S. Kheawhom and M. Y. Choi, Deciphering Indirect Nitrite Reduction to Ammonia in High-Entropy Electrocatalysts Using In Situ Raman and X-ray Absorption Spectroscopies, *Small*, 2024, **20**, 2400538.

57 T. Jiang, X. Jiang, J. Hnát, A. Michalcova, I. Biswas, R. Reissner, V. Kyriakou, F. Razmjooei, H. Liao, K. Bouzek and S.-A. Ansar, One step electrochemical fabrication of high performance Ni@Fe-doped Ni(oxy)hydroxide anode for practical alkaline water electrolysis, *J. Mater. Chem. A*, 2022, **10**, 23863–23873.

58 Y. Tong and P. Chen, Optimized hierarchical nickel sulfide as a highly active bifunctional catalyst for overall water splitting, *Dalton Trans.*, 2021, **50**, 7776–7782.

This journal is © The Royal Society of Chemistry 2025

J. Mater. Chem. A, 2025, **13**, 9073–9087 | **9087**